Electronic Supplementary Material (ESI) for Organic Chemistry Frontiers.


# Supporting Information

## Entropy Effect in Temperature-Regulated Nickel-Catalyzed Regiodivergent Alkene Hydroalkylation

Deguang Liu,[a] Jia-Wang Wang,[b] Xi Lu,*[,a] and Yao Fu*[,a]

[a] Department of Applied Chemistry, University of Science and Technology of China, Hefei 230026, China

[b] School of Plant Protection, Anhui Agricultural University, Hefei 230036, China

E-mails: luxi@mail.ustc.edu.cn (X. Lu); fuyao@ustc.edu.cn (Y. Fu)

# Contents

## Computational Methods

All calculations were performed with Gaussian 16, Rev. C01.[1] Unless specified otherwise, geometry optimizations were computed with default convergence thresholds and without symmetry constraints using the PBE0[2] density functional, augmented with Grimme's D3 empirical dispersion term at 298K.[3] The def2-SVP[4] basis set (including related effective core potential) was employed on all atoms. Frequency analysis was performed at the same level of theory with the geometry optimization to confirm that the optimized structures are local minima or transition states, and to gain the thermal correction to Gibbs free energy. Single-point energy calculations were conducted based on the optimized structures at the PBE0-D3/def2-TZVP level. The solvent effects were taken into account in all calculations by employing the SMD[5] (*N,N*-Dimethylacetamide) solvation model. The intrinsic reaction coordinate (IRC)[6] calculations were performed to ensure that the transition state connects the correct reactants and products. The geometries of the optimized structures are drawn with CYLview.[7] The free energy data at different temperatures are based on the data obtained above at 298 K, and then used Shermo 2.3.4[8], Multiwfn [9] and GoodVibes[10] (https://github.com/patonlab/GoodVibes) to obtained.

# Thermodynamic data for Ni-H generation

Hydrosilane can convert Ni-X (X=Br, I, etc.) species into the corresponding Ni-H species. This conversion will become thermodynamically favorable with the aid of $K_3PO_4$. The corresponding results are displayed in Figure S1.

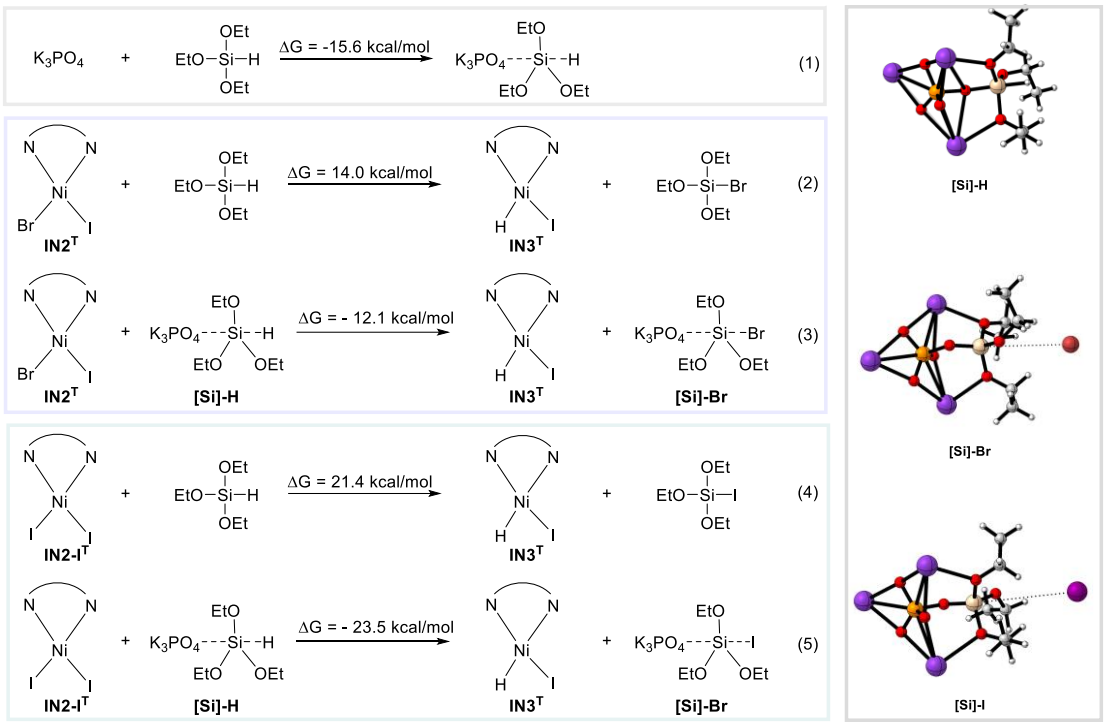


**Figure S1.** Gibbs free energy profiles of the formation to Ni-H species (298 K).

## Gibbs free energy profiles at 273 K.

For clarity, the Gibbs free energy profile of Ni/bisoxazoline catalyzed hydroalkylation at 273 K was also indicated separately in Figure S2. Of these, the processes from **TS3** to **IN7** are also labeled, which are performed prior to the selectivity determination step.

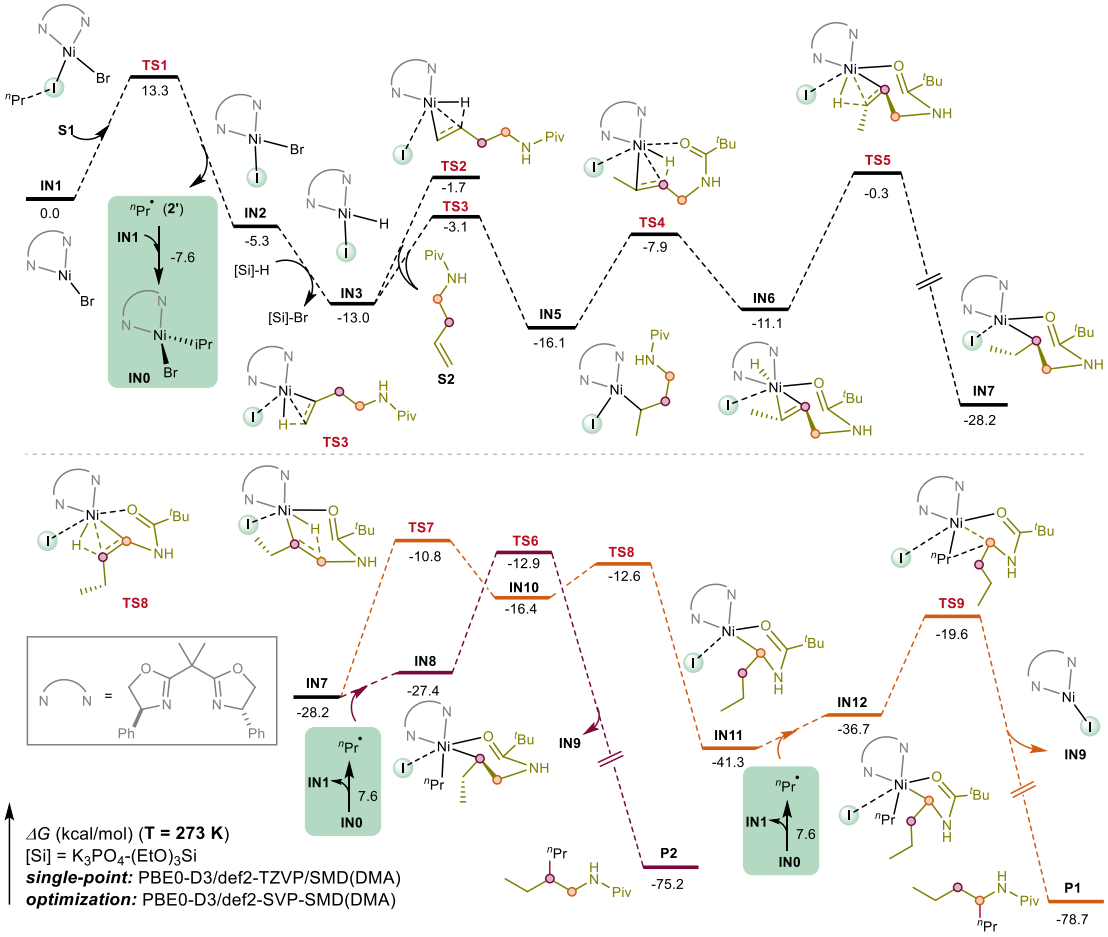


**Figure S2.** Gibbs free energy profiles of Ni/bisoxazoline catalyzed hydroalkylation at 273 K.

## Gibbs free energy profiles at 373 K.

For clarity, the Gibbs free energy profile of Ni/bisoxazoline catalyzed hydroalkylation at 373 K was indicated separately in Figure S3, where the reaction does preferentially undergo an α-H activation step, ultimately yielding the α-alkylated species.

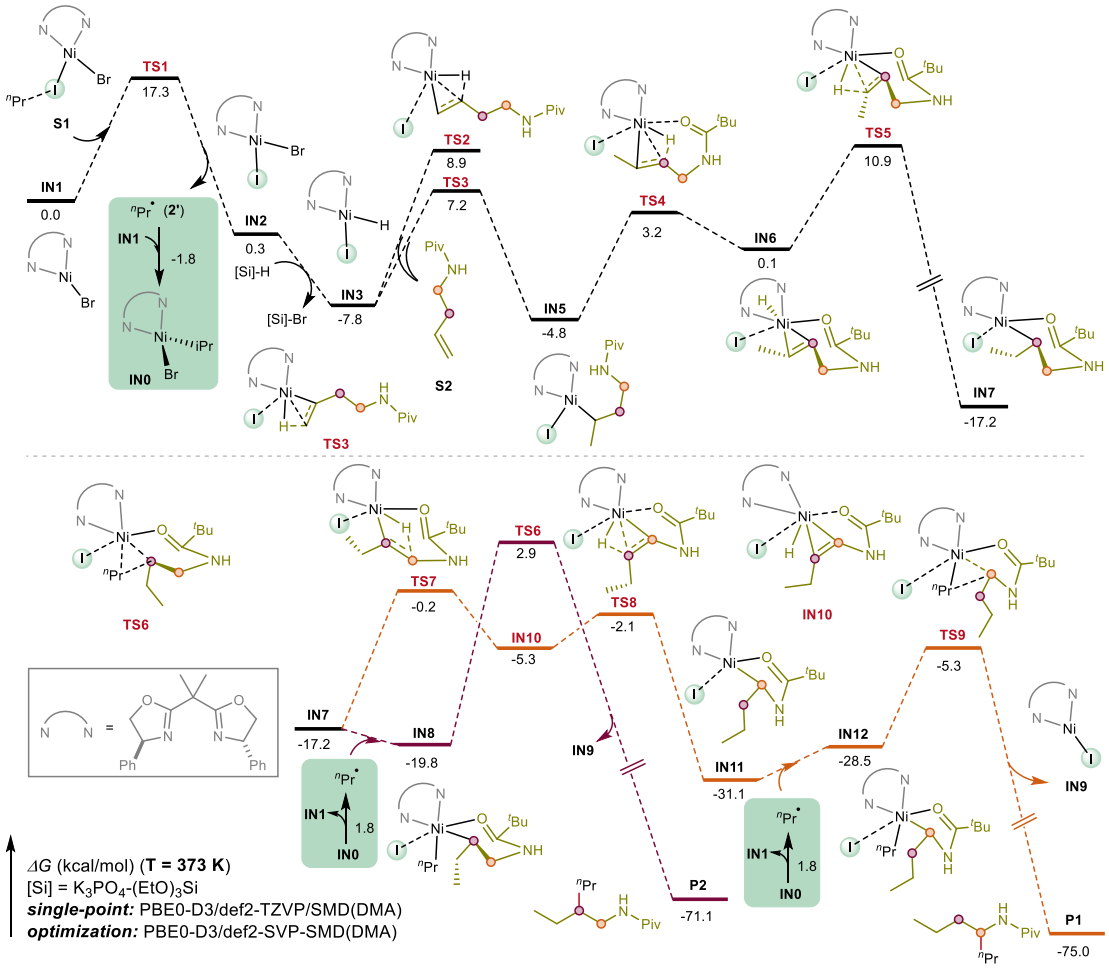


**Figure S3.** Gibbs free energy profiles of Ni/bisoxazoline catalyzed hydroalkylation at 373 K.

## Gibbs free energy profiles from IN9 to IN3.

With caution, we tested the energy profile when starting from **IN9** (unlike **IN1**, iodine replaces bromine as the starting species) to get the same hydrometallation precursor **IN3**, and the results are shown below. The results are similar to the Br case and suggest that the difference in halide does not change any reactivity.

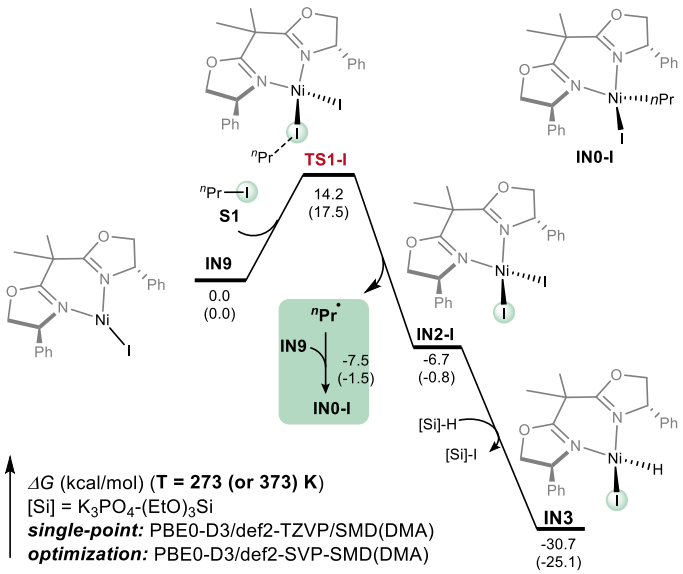


**Figure S4.** Gibbs free energy profiles from **IN9** to the hydrometallation precursor **IN3** at 273 K, the data for 373K are in brackets.

## Coordination Exchange

In the manuscript, a radical transfer strategy between **IN0** and **IN7** or **IN11** has been proposed, but we had no direct experimental evidence that such a disproportionation step necessarily occurs (**IN0**$^{(II)}$ + **IN7**$^{(II)}$ → **IN8**$^{(III)}$ + **IN1**$^{(I)}$). Therefore, the other potential solutions such as the form of ligand exchange are also worth investigating. For the sake of rigor, we also compared the case where charge transfer occurs simultaneously with the ligand exchange, and the related results are shown in Figure S2. It is apparent that both neutral and ionic ligand exchange steps are thermodynamically unfavorable and the subsequent reductive elimination is relatively challenging. Therefore, we consider that this exchange between the alkyl radicals in **IN0** and the iodide ions in **IN7** or **IN11** were unreasonable due to the unfavorable thermodynamics and kinetics of the subsequent reductive elimination.

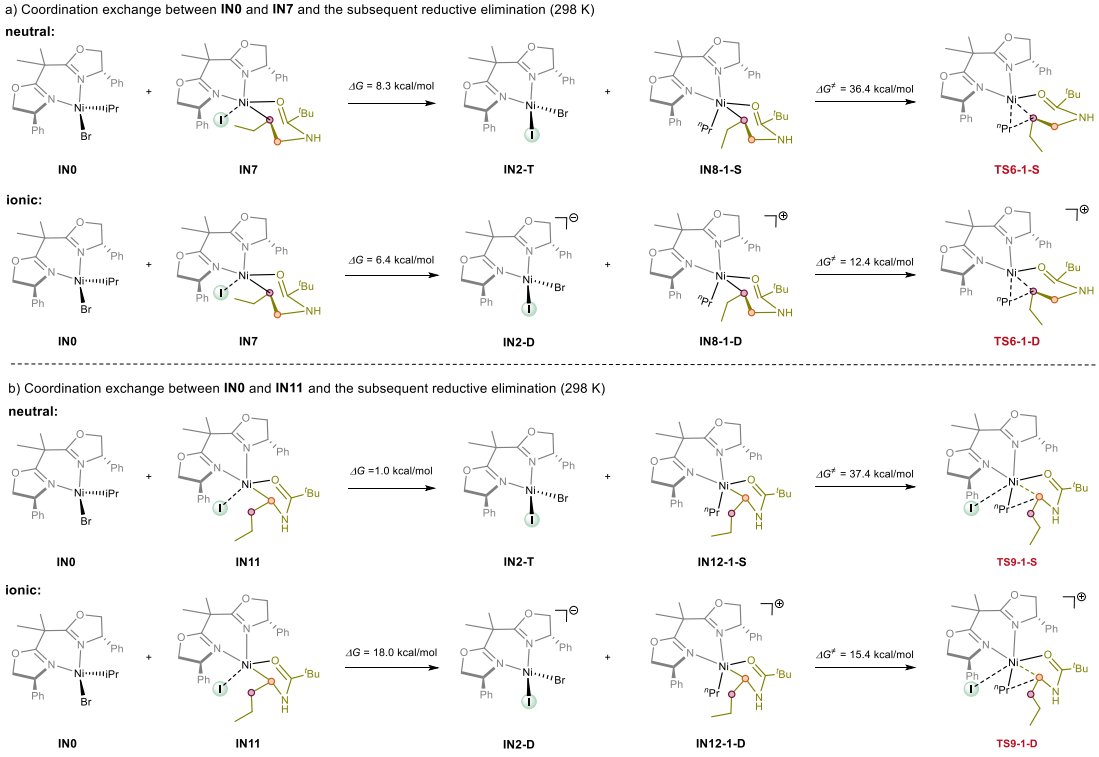


**Figure S5.** Coordination exchange between **IN0** and **IN7** or **IN11**.

## Electronic effect analysis

In order to thoroughly explore the competitive mechanism of the reductive elimination and α-H activation steps, we performed a detailed calculative analysis of the involved transition states and intermediates (Figure 6). Firstly, for Ni-H migration (α-H activation & hydrometallation *II*), it was always exothermic over the simulated temperature range (from **IN7** to **IN11**). This indicated that the step is thermodynamically driven and consistent with the experimental conclusion that increased temperature favors α-H activation (Figure 6a). Then, with the intention of investigating the effects of electronic and steric properties besides entropic effects induced with temperature, the distortion/interaction energy analysis was carried out to characterize the differences between **TS6** and **TS7** (Figure 6b).[11] In this scenario, we disassembled the transition state structures into three parts (displayed as different colors). The electronic energy barrier ($\Delta E^{\neq}$) was divided into the distortion energy ($\Delta E_{\text{dist}}$) of the three fragments to reach their transition state geometries and the interaction energy ($\Delta E_{\text{int}}$) between the fragments as shown in eq. 1.

$$\Delta E^{\neq} = \Delta E_{dist} + \Delta E_{int} \qquad (eq.1)$$

Since the *n*Pr fragment is not available in **TS7**, we assume that the fragment is freestanding. Namely, for **TS7**, the distortion and interaction energies brought out by this fragment are both zero. The correlation results indicated that **TS7** possesses a higher amide fragment distortion, which might mainly originate from the C-H bond cleavage in the α-H activation step. Therefore, we suggest that the advantage of reductive elimination at low temperatures (273 K) arises from the smaller amide fragment distortion, which is also consistent with the difficulty of α-H activation. Subsequently, we also performed the energy decomposition analysis (EDA) of the key transition states of the two reductive elimination steps (**TS6** and **TS9**), the identical steps bring comparability to the analysis.

Incidentally, both of them are almost uniformly affected by temperature, which hints at the plausibility of analyzing the electronic energies directly.Drawing on the torsion/interaction energy analysis, and with the *sobEDA* program,[12] the interaction energy ($\Delta E_{int}$) is dissected into six parts: electrostatics ($\Delta E_{els}$), exchange interaction ($\Delta E_{ex}$), DFT correlation ($\Delta E_{DFTc}$), Pauli repulsion ($\Delta E_{rep}$), orbital interaction ($\Delta E_{orb}$) and dispersion correction ($\Delta E_{dc}$) according to the following eq. 2:

$$\Delta E_{int} = \Delta E_{els} + \Delta E_{ex} + \Delta E_{DFTc} + \Delta E_{rep} + \Delta E_{orb} + \Delta E_{dc} \qquad (eq.2)$$

Referring to the strategy of Liu et al.,[13] these energies were combined according to the eq. 3:

$$\Delta E^{\neq} = \underbrace{\Delta E_{dist} + \Delta E_{rep}}_{\text{steric effects } (\Delta E_{steric})} + \overbrace{\Delta E_{els} + \Delta E_{orb}}^{\text{electronic effects } (\Delta E_{elec})} + \underbrace{\Delta E_{dc} + \Delta E_{DFTc}}_{\text{coulomb correlation } (\Delta E_{c})} \qquad \text{(eq.3)}$$

The EDA results displayed in Figure 6c suggest that the lower energy of **TS9** is mainly due to more favorable steric effects ($\Delta E_{\text{steric}}$). Among the steric effects, Pauli repulsion ($\Delta E_{\text{rep}}$) is the dominant element, which hints at more favorable inter-fragment electronic steric repulsion energies for the reductive elimination of the transition state with the five-membered Ni-amide structure. In addition, we also examined the coordination environments of Ni center in the involved transition state via the *SambVca 2.1* program,[14] and the corresponding results are displayed in Figure 6d. Generally, the buried volume of the transition state of the reductive elimination step is smaller than that of the Ni-H migration step. This is consistent with the results in Figure 6b, suggesting a steric advantage. Wherein, the smaller buried volume of **TS9** (vs **TS6**) is also consistent with the more favorable steric effects ($\Delta E_{\text{steric}}$) in Figure 6c. This is mainly reflected in the SW quadrant, where steric resistance is mainly derived from amide fragments.

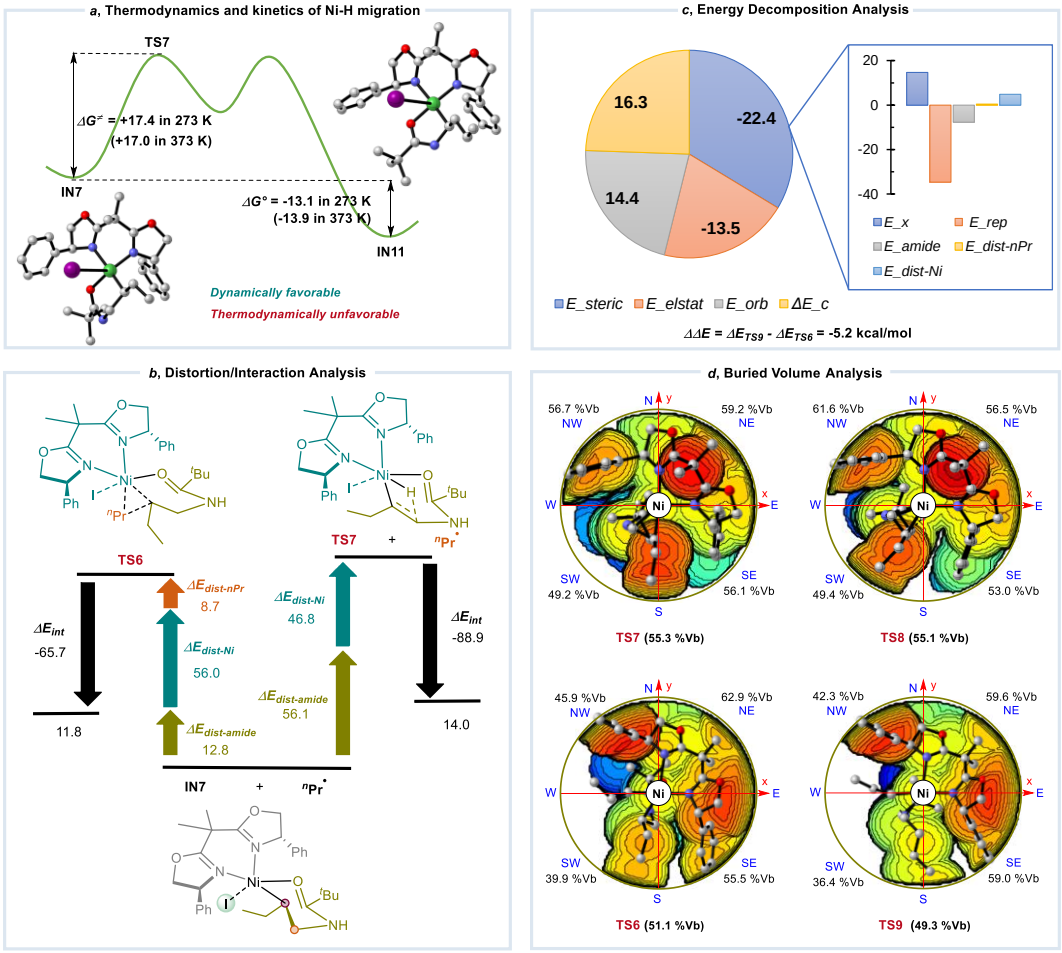


**Figure S6.** Decomposition analysis of the selectivity determining step.

## The Distortion/Interaction Analysis

With reference to the scenario proposed by Houk et al.,[11b] we performed the fragmentation of the relevant transition states, as shown in Figure S3. Therein, the energy is calculated at the level of PBE0-D3/def2-TZVP. As the *n*Pr fragment is missing in **TS7**, we additionally introduced the free *n*Pr radical as a counting that does not interact with any of the other two fragments. Of course, the fragment itself does not have a distortion energy.

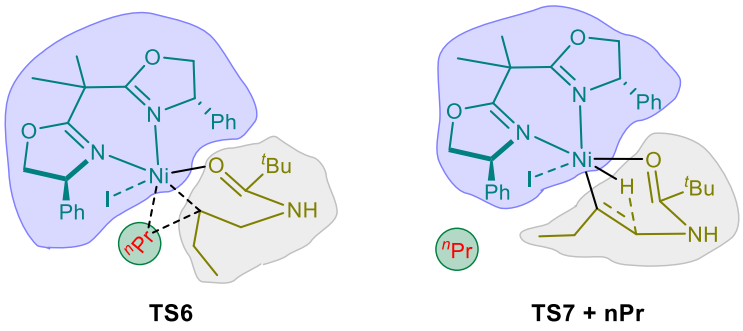


**Figure S7.** Fragmentation schemes in distortion/interaction energy analysis

## The Energy Decomposition Analysis

The energy decomposition analysis (EDA) was carried out with the sobEDA[12] and Multiwfn[9] program, with the computational level PBE0-D3/def2-TZVP. The relevant operation steps and some input information are shown below:

**Operation steps:**

(1) Put *sobEDA.sh* in any directory and add executable permissions to it with the command chmod +x [file path];

(2) Modify the settings in *sobEDA.sh* appropriately according to the actual situation;

(3) Save the structure of the whole system as *system.xyz* and put it in the current directory;

(4) Create *fragment.txt* in the current directory, and define the atomic number, net charge, and spin multiplicity of each fragment in it;

(5) Create *template.gjf* in the current directory as a template file for *sobEDA.sh* to generate Gaussian input files;

(6) Enter the path to the sobEDA.sh script to start it.

After sobEDA.sh is started, it will automatically invoke Gaussian and Multiwfn to calculate, extract and process the data, and finally output the result on the screen.

**The input information for the template.gjf:**

*#p PBE1PBE/def2TZVP EM=GD3 ExtraLinks=L608 nosymm*

*opted geometry*

*0 2*
*[geometry]*

*-13 5*

## The Buried Volume Analysis

The buried volume analysis was carried out with the Sambvca2.1[14] program (https://www.molnac.unisa.it/OMtools/sambvca2.1/index.html). The specific operation is as follows:

After loading the structure, the Ni atom was centered, the Ni-P bond was the x-axis direction, and the direction perpendicular to the ligand plane was defined as the z-axis (actually the direction via the Ni-I bond). In the subsequent parameterization, the atomic radius was chosen as Bondi radii, Sphere radius was set to 5.0, and default values were used for all other parameters.

## Thermodynamic Correction

Shermo[8] and Gaussian[1] programs were used to calculate molecular thermodynamic data at different temperatures as follows:

1. Edit the *settings.ini* file in the Shermo directory with the text editor and change the value after E= to the electronic energy of the structure.

2. Set the value after T= to the target temperature, which represents the temperature at which the analysis will be performed.

3. Set the prtvib value in *settings.ini* to -1 to output the results to *vibcontri.txt* in the current directory.

The above process was carried out via a python script written to enable batch calculations and data manipulation.

We performed a comprehensive calculation of the thermal correction to $\Delta G$ per 10 K gradient over the range 283 K to 373 K. The relevant data are displayed in Table S1, and these data distributions help us to understand the trends in reaction selectivity accompanying changes in temperature.

**Table S1.** Thermal correction to Gibbs Free Energy at different temperatures

| File Name | 283 K | 293 K | 303 K | 313 K | 323 K |
|---|---|---|---|---|---|
| **S1** | 0.0653 | 0.0640 | 0.0628 | 0.0616 | 0.0603 |
| **S2** | 0.2105 | 0.2087 | 0.2068 | 0.2049 | 0.2030 |
| **nPr** | 0.0628 | 0.0617 | 0.0606 | 0.0595 | 0.0584 |
| **P1** | 0.3126 | 0.3104 | 0.3082 | 0.3059 | 0.3035 |
| **P2** | 0.3151 | 0.3130 | 0.3108 | 0.3086 | 0.3063 |
| **IN0** | 0.4335 | 0.4304 | 0.4273 | 0.4241 | 0.4209 |
| **IN1** | 0.3390 | 0.3361 | 0.3331 | 0.3301 | 0.3271 |
| **IN2** | 0.3384 | 0.3354 | 0.3323 | 0.3291 | 0.3259 |
| **IN3** | 0.3494 | 0.3466 | 0.3437 | 0.3407 | 0.3377 |
| **IN4** | 0.5903 | 0.5864 | 0.5825 | 0.5785 | 0.5745 |
| **IN5** | 0.5932 | 0.5895 | 0.5857 | 0.5818 | 0.5779 |

| | | | | | |
|---|---|---|---|---|---|
| **IN6** | 0.5895 | 0.5857 | 0.5819 | 0.5780 | 0.5740 |
| **IN7** | 0.5921 | 0.5883 | 0.5844 | 0.5805 | 0.5765 |
| **IN8** | 0.6790 | 0.6748 | 0.6705 | 0.6662 | 0.6617 |
| **IN9** | 0.3393 | 0.3364 | 0.3335 | 0.3305 | 0.3275 |
| **IN10** | 0.5872 | 0.5835 | 0.5796 | 0.5757 | 0.5717 |
| **IN11** | 0.5881 | 0.5841 | 0.5801 | 0.5761 | 0.5719 |
| **IN12** | 0.6794 | 0.6753 | 0.6710 | 0.6667 | 0.6623 |
| **[Si]-Br** | 0.1741 | 0.1710 | 0.1678 | 0.1646 | 0.1614 |
| **[Si]-H** | 0.1858 | 0.1830 | 0.1801 | 0.1772 | 0.1742 |
| **TS1** | 0.4225 | 0.4190 | 0.4155 | 0.4119 | 0.4082 |
| **TS2** | 0.5849 | 0.5811 | 0.5772 | 0.5732 | 0.5691 |
| **TS3** | 0.5837 | 0.5799 | 0.5759 | 0.5719 | 0.5678 |
| **TS4** | 0.5872 | 0.5835 | 0.5796 | 0.5757 | 0.5717 |
| **TS5** | 0.5883 | 0.5845 | 0.5807 | 0.5768 | 0.5728 |
| **TS6** | 0.6794 | 0.6753 | 0.6711 | 0.6668 | 0.6624 |
| **TS7** | 0.5846 | 0.5808 | 0.5769 | 0.5729 | 0.5688 |
| **TS8** | 0.5844 | 0.5805 | 0.5766 | 0.5726 | 0.5685 |
| **TS9** | 0.6775 | 0.6733 | 0.6690 | 0.6646 | 0.6601 |

**continued**

| **File Name** | **333 K** | **343 K** | **353 K** | **363 K** | **373 K** |
|---|---|---|---|---|---|
| **S1** | 0.0590 | 0.0577 | 0.0564 | 0.0551 | 0.0538 |
| **S2** | 0.2010 | 0.1990 | 0.1970 | 0.1950 | 0.1929 |
| **nPr** | 0.0573 | 0.0561 | 0.0550 | 0.0538 | 0.0526 |
| **P1** | 0.3012 | 0.2988 | 0.2963 | 0.2939 | 0.2914 |
| **P2** | 0.3040 | 0.3017 | 0.2993 | 0.2969 | 0.2945 |
| **IN0** | 0.4176 | 0.4143 | 0.4108 | 0.4074 | 0.4038 |
| **IN1** | 0.3240 | 0.3209 | 0.3177 | 0.3144 | 0.3111 |
| **IN2** | 0.3226 | 0.3193 | 0.3159 | 0.3125 | 0.3090 |
| **IN3** | 0.3347 | 0.3316 | 0.3284 | 0.3252 | 0.3220 |
| **IN4** | 0.5703 | 0.5661 | 0.5618 | 0.5574 | 0.5530 |
| **IN5** | 0.5738 | 0.5697 | 0.5655 | 0.5612 | 0.5569 |

| | | | | | |
|---|---|---|---|---|---|
| **IN6** | 0.5700 | 0.5658 | 0.5616 | 0.5573 | 0.5529 |
| **IN7** | 0.5724 | 0.5682 | 0.5640 | 0.5596 | 0.5552 |
| **IN8** | 0.6572 | 0.6526 | 0.6479 | 0.6431 | 0.6382 |
| **IN9** | 0.3244 | 0.3212 | 0.3180 | 0.3148 | 0.3115 |
| **IN10** | 0.5676 | 0.5635 | 0.5592 | 0.5549 | 0.5505 |
| **IN11** | 0.5677 | 0.5634 | 0.5590 | 0.5545 | 0.5499 |
| **IN12** | 0.6577 | 0.6531 | 0.6484 | 0.6437 | 0.6388 |
| **[Si]-Br** | 0.1581 | 0.1547 | 0.1513 | 0.1479 | 0.1444 |
| **[Si]-H** | 0.1712 | 0.1681 | 0.1650 | 0.1619 | 0.1587 |
| **TS1** | 0.4045 | 0.4007 | 0.3968 | 0.3929 | 0.3889 |
| **TS2** | 0.5649 | 0.5607 | 0.5564 | 0.5520 | 0.5475 |
| **TS3** | 0.5636 | 0.5593 | 0.5550 | 0.5506 | 0.5461 |
| **TS4** | 0.5676 | 0.5634 | 0.5592 | 0.5548 | 0.5504 |
| **TS5** | 0.5688 | 0.5646 | 0.5604 | 0.5561 | 0.5518 |
| **TS6** | 0.6580 | 0.6534 | 0.6488 | 0.6440 | 0.6392 |
| **TS7** | 0.5646 | 0.5604 | 0.5561 | 0.5517 | 0.5472 |
| **TS8** | 0.5644 | 0.5601 | 0.5558 | 0.5514 | 0.5469 |
| **TS9** | 0.6555 | 0.6509 | 0.6461 | 0.6413 | 0.6364 |

## Calculated Energies

$$G_{sol} = \Delta E_{sol} + G_{corr}$$

$E_{sol}$ refers to the single point energy involved with solvent effects by PBE0-D3/def2-TZVP/SMD (*N,N*-Dimethylacetamide).

$G_{corr}$ refers to the thermal correction to the Gibbs free energy calculated at PBE0-D3/def2-SVP/SMD (*N,N*-Dimethylacetamide) level of theory.

$G_{sol}$ refers to the sum of the solvation single point energy and the thermal correction to the Gibbs free energy.

Table S2 presented the raw computational data (298 K) for the relevant structures involved in the manuscript, with the superscript S, D, T and Q denoting the singlet, doublet, triplet, and quartet states, respectively.

**Table S2.** The $G_{corr}$, $E_{sol}$ and $G_{sol}$ of Optimized Structures

| Number | $G_{corr}$(Hartree) | $E_{sol}$(Hartree) | $G_{sol}$(kcal/mol) |
|---|---|---|---|
| **IN0A$^{D}$** | 0.6605 | -3182.0012 | -1996321.19 |
| **IN0B$^{D}$** | 0.4230 | -7847.0161 | -4923810.96 |
| **IN0B$^{Q}$** | 0.4136 | -7846.9987 | -4923805.95 |
| **IN0$^{S}$** | 0.4289 | -5273.1095 | -3308656.69 |
| **IN0$^{T}$** | 0.4223 | -5273.1148 | -3308664.12 |
| **IN10$^{S}$** | 0.5812 | -3361.9742 | -2109305.71 |
| **IN11$^{S}$** | 0.5822 | -3362.0153 | -2109325.34 |
| **IN11$^{S}$** | 0.5822 | -3362.0153 | -2109330.90 |
| **IN12-1$^{D}$** | 0.6800 | -3182.5002 | -1996622.03 |
| **IN12-1$^{Q}$** | 0.6675 | -3182.4631 | -1996606.65 |
| **IN12-1$^{S}$** | 0.6735 | -3182.6158 | -1996698.70 |
| **IN12-1$^{T}$** | 0.6688 | -3182.5942 | -1996688.11 |
| **IN12$^{D}$** | 0.6732 | -3480.4101 | -2183567.66 |
| **IN12$^{D}$** | 0.6732 | -3480.4101 | -2183567.66 |
| **IN1A$^{S}$** | 0.5739 | -3063.5887 | -1922070.60 |
| **IN1B$^{S}$** | 0.3360 | -7728.6182 | -4849569.77 |
| **IN1B$^{T}$** | 0.3332 | -7728.6296 | -4849578.62 |

| | | | |
|---|---|---|---|
| **IN1$^{D}$** | 0.3346 | -5154.7035 | -3234414.93 |
| **IN1$^{Q}$** | 0.3324 | -5154.6323 | -3234371.66 |
| **IN2$^{D}$** | 0.3327 | -5452.6095 | -3421355.00 |
| **IN2$^{Q}$** | 0.3305 | -5452.5541 | -3421321.54 |
| **IN2$^{S}$** | 0.3402 | -5452.4893 | -3421274.83 |
| **IN2$^{T}$** | 0.3338 | -5452.4945 | -3421282.06 |
| **IN3$^{S}$** | 0.3451 | -2879.1393 | -1806470.38 |
| **IN3$^{T}$** | 0.3402 | -2879.1410 | -1806474.62 |
| **IN7$^{S}$** | 0.5864 | -3361.9984 | -2109317.63 |
| **IN8-1$^{D}$** | 0.6791 | -3182.4966 | -1996620.35 |
| **IN8-1$^{Q}$** | 0.6728 | -3182.4635 | -1996603.57 |
| **IN8-1$^{S}$** | 0.6767 | -3182.6073 | -1996691.35 |
| **IN8-1$^{T}$** | 0.6691 | -3182.5874 | -1996683.64 |
| **IN8$^{D}$** | 0.6727 | -3480.4070 | -2183566.03 |
| **IN9$^{D}$** | 0.3350 | -2878.5706 | -1806119.90 |
| **nPr** | 0.0612 | -118.3632 | -74235.60 |
| **[Si]-Br** | 0.1694 | -5768.1245 | -3619446.06 |
| **[Si]-H** | 0.1815 | -3194.7577 | -2004626.58 |
| **P1** | 0.3093 | -601.8809 | -377491.81 |
| **P2** | 0.3119 | -601.8778 | -377488.28 |
| **S1** | 0.0634 | -416.1607 | -261110.57 |
| **S2** | 0.2077 | -482.8037 | -302833.52 |
| **TS1$^{D}$** | 0.4165 | -5570.8607 | -3495506.07 |
| **TS3$^{S}$** | 0.5783 | -3361.9502 | -2109292.46 |
| **TS3$^{T}$** | 0.5767 | -3361.9426 | -2109288.71 |
| **TS6-1$^{D}$** | 0.6790 | -3182.4766 | -1996607.90 |
| **TS6-1$^{S}$** | 0.6738 | -3182.5463 | -1996654.91 |
| **TS6-1$^{T}$** | 0.6721 | -3182.5211 | -1996640.11 |
| **TS6$^{D}$** | 0.6743 | -3480.3806 | -2183548.39 |
| **TS7$^{S}$** | 0.5787 | -3361.9567 | -2109300.75 |
| **TS8$^{S}$** | 0.5774 | -3361.9569 | -2109303.15 |
| **TS9-1$^{D}$** | 0.6766 | -3182.4721 | -1996606.61 |

| | | | |
|---|---|---|---|
| **TS9-1$^{Q}$** | 0.6742 | -3182.4139 | -1996571.58 |
| **TS9-1$^{S}$** | 0.6698 | -3182.5525 | -1996661.27 |
| **TS9-1$^{T}$** | 0.6717 | -3182.5252 | -1996643.00 |
| **TS9$^{D}$** | 0.6694 | -3480.3819 | -2183552.30 |

## Selectivity Data

Experimentally relevant data covered in the manuscript are displayed in the Table S3, with original data from previous reports.[15]

**Table S3.** The values of α-selectivity and β-selectivity in the experiment (kcal/mol)

| T(K) | α-Selectivity | β-Selectivity | *r.r value* | $\Delta\Delta G_{experimental}$ |
|---|---|---|---|---|
| 283 | 7.28 | 75.72 | 0.10 | -2.59 |
| 293 | 18.51 | 68.49 | 0.27 | -1.47 |
| 303 | 35.32 | 53.68 | 0.66 | -0.49 |
| 313 | 45.37 | 43.63 | 1.04 | 0.05 |
| 323 | 78.06 | 13.94 | 5.60 | 2.07 |
| 333 | 87.94 | 6.06 | 14.51 | 3.27 |
| 343 | 91.88 | 2.12 | 43.34 | 4.69 |
| 353 | 93.56 | 1.44 | 64.97 | 5.27 |
| 363 | 94.84 | 1.16 | 81.76 | 5.65 |

Table S4 lists the data for the relevant calculations involved in the manuscript, which include $\Delta\Delta$G in the linear fit, and enthalpy and entropy at the corresponding temperatures. From the data, it is apparent that there is a small change in $\Delta\Delta$H and a large change in T$\Delta\Delta$S, with this item dominating the trend of $\Delta\Delta$G.

**Table S4.** The values of α-selectivity and β-selectivity in the experiment

| T(K) | $\Delta\Delta$G | $\Delta\Delta$H | $\Delta\Delta$S | -T$\Delta\Delta$S |
|---|---|---|---|---|
| 273 | -2.11 | -16.08 | -0.05 | 13.97 |
| 283 | -1.60 | -16.12 | -0.05 | 14.52 |
| 293 | -1.08 | -16.15 | -0.05 | 15.07 |

| | | | | |
|---|---|---|---|---|
| 303 | -0.57 | -16.18 | -0.05 | 15.61 |
| 313 | -0.05 | -16.22 | -0.05 | 16.16 |
| 323 | 0.46 | -16.25 | -0.05 | 16.71 |
| 333 | 0.98 | -16.28 | -0.05 | 17.26 |
| 343 | 1.50 | -16.31 | -0.05 | 17.81 |
| 353 | 2.02 | -16.34 | -0.05 | 18.36 |
| 363 | 2.54 | -16.37 | -0.05 | 18.91 |
| 373 | 3.06 | -16.40 | -0.05 | 19.46 |

# Reference


(1) M. J. Frisch, G. W. T., H. B. Schlegel, G. E. Scuseria, M. A. Robb, J. R. Cheeseman, G. Scalmani, V. Barone, G. A. Petersson, H. Nakatsuji, X. Li, M. Caricato, A. V. Marenich, J. Bloino, B. G. Janesko, R. Gomperts, B. Mennucci, H. P. Hratchian, J. V. Ortiz, A. F. Izmaylov, J. L. Sonnenberg, D. Williams-Young, F. Ding, F. Lipparini, F. Egidi, J. Goings, B. Peng, A. Petrone, T. Henderson, D. Ranasinghe, V. G. Zakrzewski, J. Gao, N. Rega, G. Zheng, W. Liang, M. Hada, M. Ehara, K. Toyota, R. Fukuda, J. Hasegawa, M. Ishida, T. Nakajima, Y. Honda, O. Kitao, H. Nakai, T. Vreven, K. Throssell, J. A. Montgomery, Jr., J. E. Peralta, F. Ogliaro, M. J. Bearpark, J. J. Heyd, E. N. Brothers, K. N. Kudin, V. N. Staroverov, T. A. Keith, R. Kobayashi, J. Normand, K. Raghavachari, A. P. Rendell, J. C. Burant, S. S. Iyengar, J. Tomasi, M. Cossi, J. M. Millam, M. Klene, C. Adamo, R. Cammi, J. W. Ochterski, R. L. Martin, K. Morokuma, O. Farkas, J. B. Foresman, and D. J. Fox Gaussian 16, Revision C.01, Gaussian, Inc., Wallingford Ct, 2019.

(2) (a) Perdew, J. P.; Burke, K.; Ernzerhof, M. Generalized Gradient Approximation Made Simple. *Phy. Rev. Lett.* **1996**, *77*, 3865-3868. (b) Elmér, R.; Berg, M.; Carlén, L.; Jakobsson, B.; Norén, B.; Oskarsson, A.; Ericsson, G.; Julien, J.; Thorsteinsen, T. F.; Guttormsen, M.; Løvhøiden, G.; Bellini, V.; Grosse, E.; Müntz, C.; Senger, P.; Westerberg, L. K+ Emission in Symmetric Heavy Ion Reactions at Subthreshold Energies. *Phy. Rev. Lett.* **1996**, *77*, 4884-4886.

(3) (a) Grimme, S.; Antony, J.; Ehrlich, S.; Krieg, H. A Consistent and Accurate Ab Initio Parametrization of Density Functional Dispersion Correction (Dft-D) for the 94 Elements H-Pu. *J. Chem. Phys.* **2010**, *132*, 154104. (b) Grimme, S.; Ehrlich, S.; Goerigk, L. Effect of the Damping Function in Dispersion Corrected Density Functional Theory. *J. Comput. Chem.* **2011**, *32*, 1456-1465.

(4) (a) Treutler, O.; Ahlrichs, R. Efficient Molecular Numerical Integration Schemes. *J. Chem. Phys.* **1995**, *102*, 346-354. (b) Weigend, F.; Ahlrichs, R. Balanced Basis Sets of Split Valence, Triple Zeta Valence and Quadruple Zeta Valence Quality for H to Rn: Design and Assessment of Accuracy. *Physical Chemistry Chemical Physics* **2005**, *7*, 3297-3305.

(5) Marenich, A. V.; Cramer, C. J.; Truhlar, D. G. Universal Solvation Model Based on Solute Electron Density and on a Continuum Model of the Solvent Defined by the Bulk Dielectric

Constant and Atomic Surface Tensions. *J. Phys. Chem. B* **2009**, *113*, 6378-6396.

(6) (a) Fukui, K. Formulation of the Reaction Coordinate. *J. Phys. Chem.* **1970**, *74*, 4161-4163. (b) Fukui, K. The Path of Chemical Reactions - the Irc Approach. *Acc. Chem. Res.* **1981**, *14*, 363-368.

(7) CYLview20; Legault, C. Y., Université de Sherbrooke, 2020 (http://www.cylview.org).

(8) Lu, T.; Chen, Q. Shermo: A General Code for Calculating Molecular Thermochemistry Properties. *Comput. Theor. Chem.* **2021**, *1200*, 113249.

(9) Lu, T.; Chen, F. Multiwfn: A Multifunctional Wavefunction Analyzer. *J. Comput. Chem.* **2012**, *33*, 580-592.

(10) Luchini, G.; Alegre-Requena, J.; Funes-Ardoiz, I.; Paton, R. Goodvibes: Automated Thermochemistry for Heterogeneous Computational Chemistry Data. *F1000Research* **2020**, *9*, 291.

(11) (a) Chen, S.; Huang, X.; Meggers, E.; Houk, K. N. Origins of Enantioselectivity in Asymmetric Radical Additions to Octahedral Chiral-at-Rhodium Enolates: A Computational Study. *J. Am. Chem. Soc.* **2017**, *139*, 17902-17907. (b) Ess, D. H.; Houk, K. N. Distortion/Interaction Energy Control of 1,3-Dipolar Cycloaddition Reactivity. *J. Am. Chem. Soc.* **2007**, *129*, 10646-10647.

(12) Lu, T.; Chen, Q. Simple, Efficient, and Universal Energy Decomposition Analysis Method Based on Dispersion-Corrected Density Functional Theory. *J. Phys. Chem. A* **2023**, *127*, 7023-7035.

(13) Qi, X.; Kohler, D. G.; Hull, K. L.; Liu, P. Energy Decomposition Analyses Reveal the Origins of Catalyst and Nucleophile Effects on Regioselectivity in Nucleopalladation of Alkenes. *J. Am. Chem. Soc.* **2019**, *141*, 11892-11904.

(14) Falivene, L.; Cao, Z.; Petta, A.; Serra, L.; Poater, A.; Oliva, R.; Scarano, V.; Cavallo, L. Towards the Online Computer-Aided Design of Catalytic Pockets. *Nat. Chem.* **2019**, *11*, 872-879.

(15) Wang, J.-W.; Liu, D.-G.; Chang, Z.; Li, Z.; Fu, Y.; Lu, X. Nickel-Catalyzed Switchable Site-Selective Alkene Hydroalkylation by Temperature Regulation. *Angew. Chem. Int. Ed.* **2022**, *61*, e202205537.